catalysts

MDPI

Article

Effective Electron Transfer Pathway of the Ternary TiO_2/RGO/Ag Nanocomposite with Enhanced Photocatalytic Activity under Visible Light

Hongwei Tian [1,*], Chenxing Wan [1], Xin Xue [2], Xiaoying Hu [3] and Xiaoyi Wang [4,*]

1 Department of Materials Science and Key Laboratory of Automobile Materials of MOE, Jilin University, Changchun 130012, China; w626374440@163.com
2 The Second Hospital, Jilin University, Changchun 130041, China; xuexinsir@163.com
3 College of Science, Changchun University, Changchun 130022, China; huxy@ccu.edu.cn
4 Key Laboratory of Optical System Advanced Manufacturing Technology, Changchun Institute of Optics, Fine Mechanics and Physics, Chinese Academy of Sciences, Changchun 130033, China
* Correspondence: tianhw@jlu.edu.cn (H.T.); wangxiaoyi1977@sina.com (X.W.); Tel.: +86-0431-8516-8444 (H.T.); +86-0431-8670-8126 (X.W.)

Academic Editors: Shaobin Wang and Xiaoguang Duan
Received: 24 March 2017; Accepted: 10 May 2017; Published: 15 May 2017

Abstract: Mesoporous TiO_2/reduced graphene oxide/Ag (TiO_2/RGO/Ag) ternary nanocomposite with an effective electron transfer pathway is obtained by an electrostatic self-assembly method and photo-assisted treatment. Compared with bare mesoporous TiO_2 (MT) and mesoporous TiO_2/RGO (MTG), the ternary mesoporous TiO_2/RGO/Ag (MTGA) nanocomposite exhibited superior photocatalytic performance for the degradation of methylene blue (MB) under visible light, and the degradation rate reached 0.017 min^{-1}, which was 3.4-times higher than that of MTG. What is more, the degradation rate of MTGA nanocomposite after three cycle times is 91.2%, and the composition is unchanged. In addition, we found that the OH•, h^+ and especially $O_2^{\bullet -}$ contribute to the high photocatalytic activity of MTGA for MB degradation. It is proposed that Ag nanoparticles can form the local surface plasmon resonance (LSPR) to absorb the visible light and distract the electrons into MT, and RGO can accept the electrons from MT to accelerate the separation efficiency of photogenerated carriers. The establishment of MTGA ternary nanocomposite makes the three components act synergistically to enhance the photocatalytic performance.

Keywords: mesoporous TiO_2; reduced graphene oxide; Ag nanoparticles; photocatalytic activity; visible light irradiation

1. Introduction

As a promising wide-bandgap semiconductor material, titanium dioxide (TiO_2) has been widely applied in the field of photocatalysis [1–3]. TiO_2 photocatalyst is acknowledged as the most suitable material due to its excellent adjustable microstructure, chemical stability, non-toxicity, easy practicality and low cost [4–8]. However, there are still some defects mainly concentrated in the high recombination rate of photogenerated carriers and only absorbing UV light. The usual way for overcoming these shortcomings is coupling with sensitizing agents, narrow-bandgap semiconductor and non-metal-doping or with noble metal materials [9–15].

Graphene, a promising material with the traits of large surface area, high conductivity, good transparency and high stability, has attracted great recent attention in various fields [16–18]. Combining TiO_2 with graphene could enhance the photocatalytic capacity, which facilitates the charge separation and transportation and suppresses the recombination of photogenerated electrons and holes [19–21]. Besides graphene, the decoration of noble metal Ag could enhance the photocatalytic activity of TiO_2

photocatalysts, due to the local surface plasmon resonance (LSPR) effect for optimizing the use of solar energy and improving the transfer efficiency of photogenerated carriers [13,22–26].

In recent years, constructing a ternary structure has turned into an effective tactic to enhance the absorbing of solar light and photocatalytic capability. Xian et al. reported that the obtained TiO_2 nanotube array (TNT)-graphene (GR)-CdS quantum dot (TNT-GR-CdS) composite film revealed higher photoelectric response and photocatalytic activities than other bare TNT, TNT-CdS and TNT-GR [27]. Myilsamy et al. synthesized by the sol-gel route indium and cerium co-doped mesoporous TiO_2 nanocomposite with a shifted light absorption band-edge position to the visible region and the efficiently suppressed electron-hole recombination [28]. Li and his co-workers prepared graphene/Fe^{3+}-doped TiO_2 nanowire composites; it was found that Fe^{3+} doping could keep the more direct contact between TiO_2 and graphene and improved the response of TiO_2 nanowires [29]. To date, more similar ternary structures have appeared in pace with the higher requirement for the photocatalytic capability of materials, e.g., TiO_2/$InVO_4$/reduced graphene oxide (RGO) [30], C, N co-doping mesoporous Au/TiO_2 [31] and Ag-AgBr/TiO_2 [32].

Accordingly, combining Ag and graphene with TiO_2 to build the ternary skeleton can enhance the photocatalytic performance of TiO_2 due to the collective effect of Ag nanoparticles and graphene.

In 2011, Wen et al. came up with a new nanocomposite consisting of anatase TiO_2, Ag and graphene serving as a visible light-activated photocatalyst [33]. Then, more reports about TiO_2, Ag and graphene nanocomposites appeared, mainly focusing on synthetic methods, morphologies and applications. The synthetic methods include the microwave-assisted with hydrothermal, one-step electrochemical deposition method, the sol-gel/solvothermal method and single-step solvothermal synthesis [25,34–36]. In terms of morphologies, Zhang et al. fabricated surface-coarsened TiO_2 nanobelts enwrapped with monodispersed Ag nanoparticles and GR nanosheets, but the improved photocatalytic performances still remained in UV light [37]; Gou et al. prepared TiO_2 nanofibers/reduced graphene oxide/Ag nanoparticle nanocomposite photocatalysts with UV/Vis response properties, and the electron transfer path was Ag→RGO→TiO_2 under visible light [38]. In another aspect, Vasilaki et al. carried out a comprehensive comparison between TiO_2/Ag/RGO and other photocatalysts including bare TiO_2, TiO_2/RGO and even TiO_2/Ag [39]; Zhang et al. utilized the one-pot solvothermal method to synthesize Ag-TiO_2/reduced graphene oxide (r-GO) nanocomposite with excellent adsorbent capacity, and the Ag-TiO_2/r-GO nanocomposite displayed enhanced performance toward removal of rhodamine B (Rh B) dyes and reduction of CO_2 [40]. However, few reports formally proposed "the electron-transfer mechanism"; we put forward that a feasible electron transfer route is that Ag nanoparticles deliver the electrons to the conduction band (CB) of mesoporous TiO_2 (MT), following RGO nanosheets that can receive electrons to effectively separate electrons and holes.

In this work, we utilized an electrostatic self-assembly approach and a photo-assisted reduction process to complete the decoration of Ag nanoparticles and RGO nanosheets on the basis of mesoporous TiO_2. Compared with MT and mesoporous TiO_2/RGO (MTG), the ternary mesoporous TiO_2/RGO/Ag (MTGA) nanocomposite exhibited superior photocatalytic performance for the degradation of methylene blue (MB) under visible light irradiation, and the degradation rate reached 0.017 min^{-1}, which was 3.4-times that of MTG. What is more, the degradation rate of MTGA nanocomposite after three cycle times is 91.2%, and the composition is unchanged. In addition, we found that the OH•, h^+ and especially $O_2^{\bullet -}$ contribute to the high photocatalytic activity of MTGA for MB degradation. More importantly, the enhancement of the photocatalytic activity could be ascribed to the large specific surface area, the extensive photo response regions and the highly efficient separation and transmission of the photo-induced charge carriers caused by the feasible electron-transfer pathway.

2. Results and Discussion

Figure 1 depicts X-ray diffractometer (XRD) spectra of MT, MTG and MTGA nanocomposites, indicating that the diffraction peaks at 25.3°, 37.8°, 48.0°, 53.9°, 55.1°, 62.7°, 70.3° and 75.0° of MT

could well match with the (101), (004), (200), (105), (204), (220) and (215) planes of the anatase-phase TiO_2 (JCPDS No. 21-1272). There are no obvious diffraction peaks of RGO in the sample of MTG, duo to the low contents of RGO. After photo-assisted loaded Ag nanoparticles, there are two peaks at 38.1° and 44.2° in accordance with the typical diffraction peaks of Ag (JCPDS No. 04-0783), corresponding to the (111) and (200) planes of Ag nanoparticles. Specifically, the peak of the (111) plane is covered by TiO_2 (004), but the intensity of this peak is heightened by Ag nanoparticles compared with MT and MTG, and the intensity of another peak located at 44.2° is relatively weak because of the low doped and high dispersed of Ag nanoparticles.

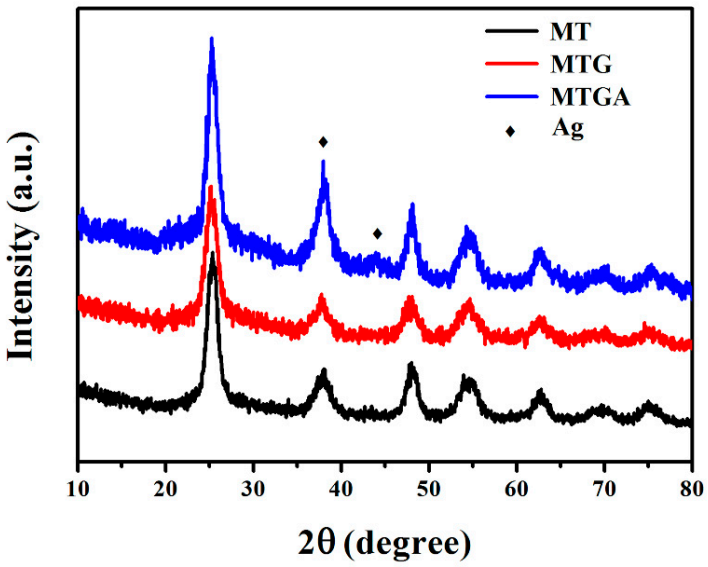

Figure 1. X-ray diffractometer (XRD) spectra of mesoporous TiO_2 (MT), mesoporous TiO_2/reduced graphene oxide (MTG) and mesoporous TiO_2/reduced graphene oxide (RGO)/Ag (MTGA).

The resulting Raman spectra of MT, MTG and MTGA nanocomposites shown in Figure 2 highlights four particular peaks owed to anatase-phase TiO_2 located at 146 (Eg), 399 (B1g), 517 (A1g) and 639 cm^{-1} (Eg), emerging in all of the samples [41]. Besides that, the inset of Figure 2 shows the Raman spectrum of GO with two manifest peaks at 1351 cm^{-1} (D-band) and 1605 cm^{-1} (G-band). The D-band originates from the disorder with structural defects caused in the process of the reduction of GO. Meanwhile, the G-band corresponds to the first order scattering of the E2g photon of sp2 C atoms of graphene [21,29]. Therefore, the intensity ratio between D-band and G-band (I_D/I_G) for GO was 0.88, signifying the existence of plentiful sp3 in the sample. The D- and G-bands of MTG and MTGA were approximately in the same position with GO. However, the I_D/I_G of MTG and MTGA decreased to 0.69 and 0.79, respectively, demonstrating the reduction of GO via the photo-assisted process [42,43].

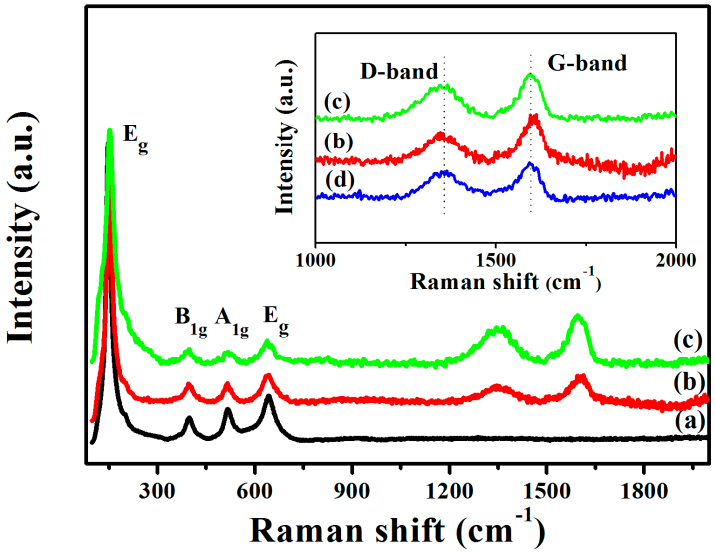

Figure 2. Raman spectra of (**a**) MT, (**b**) MTG, (**c**) MTGA and (**d**) GO (inset).

The pore structure and the Brunauer-Emmett-Teller (BET) surface area of MT, MTG and MTGA nanocomposites were evaluated by the nitrogen adsorption-desorption curves shown in Figure 3. All of the isotherms belong to type IV with the H2 hysteresis loop, which verify that the pore structure is made up of ink-bottle pores [43]. The MTGA ternary nanocomposite has a large specific surface area and suitable pore size, which are investigated respectively to be 119 m^2 g^{-1} and 6.55 nm, shown in Table S1. In a sense, the pore structure and large surface area would become principal factors for heightening the photocatalytic performance of MTGA nanocomposite.

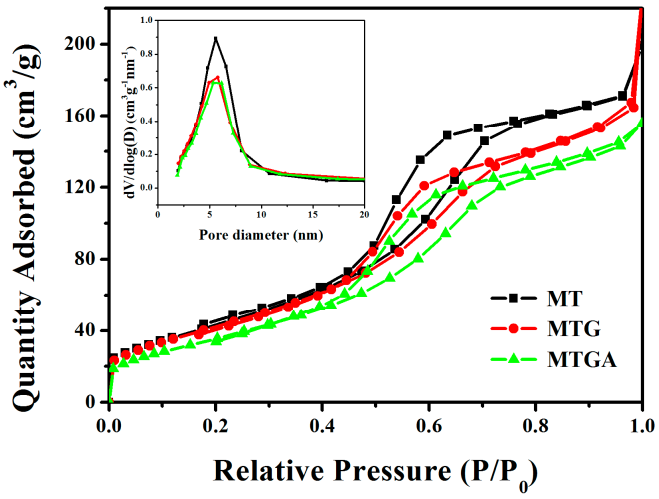

Figure 3. Nitrogen sorption isotherms and the corresponding pore size distribution curves for MT, MTG and MTGA.

The surface elemental compositions and chemical states were inspected by X-ray photoelectron spectroscopy (XPS). Figure 4 shows the existence of the elements Ti, Ag, O and C in the MTGA ternary nanocomposite. In particular, as shown in Figure 4a, Ti 2p exhibits two typical peaks situated at 459.2 and 464.9 eV, noting the state of Ti^{4+} in anatase-phase TiO_2 [44]. In Figure 4b, the two peaks at 368.35 eV and 374.1 eV for Ag 3d5/2 and Ag 3d3/2 can be assigned to metallic silver (Ag) [45]. The XPS spectrum of O 1s is divided into three peaks (532.25, 533.65 and 535.25 eV) attributed to the

Ti-O bond in the TiO_2 nanocrystal, the Ti-OH group on the surface of TiO_2 and the –COOH species from CO_2 adsorption, respectively [46]. Moreover, the fact that GO was reduced to RGO is proven by the Figure 4d–f. The XPS spectrum in Figure 4d highlights the abundance of diverse oxygen-containing functional groups, mainly including C–OH, C–O and O=C–O on the GO surface, corresponding to the peaks position at 286, 287.4 and 289 eV [47]. The attenuation of the oxygen-containing functional groups in Figure 4e,f of MTG and MTGA nanocomposites is remarkable, which certified the reduction of GO after light illumination [48–50].

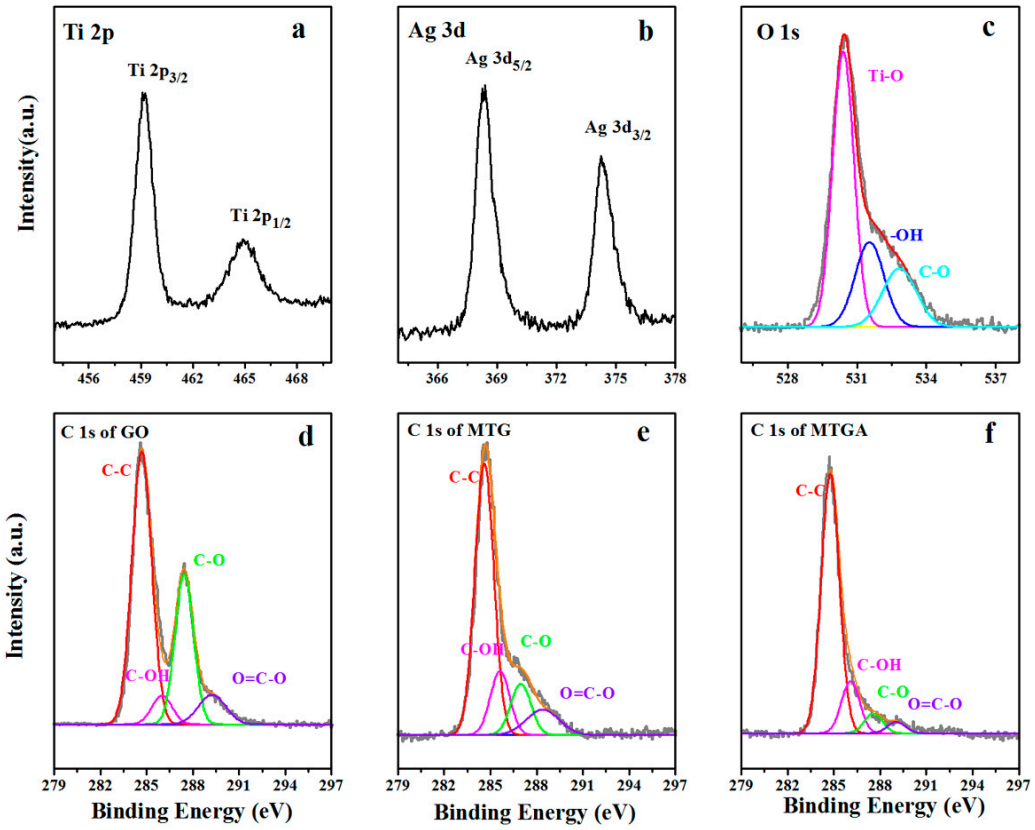

Figure 4. X-ray photoelectron spectroscopy (XPS) spectra of Ti 2p (**a**), Ag 3d (**b**) and O 1s (**c**) of the MTGA nanocomposite; XPS spectra of C 1s for GO (**d**), MTG (**e**) and MTGA (**f**).

The morphology of the MTGA nanocomposite can be characterized by field emission scanning electron microscope (FESEM) and transmission electron microscopy (TEM). Figure 5 shows SEM images of MT, MTG and a series of MTGA nanocomposites with different amounts of Ag nanoparticles. MT in Figure 5a is agglomerated into a block, and no other particles are attached to its surface. When combining MT with RGO nanosheets, as shown in Figure 5b, we find that MT is intimately enwrapped by RGO nanosheets, suggesting efficient self-assembly of RGO on the surface of MT via electrostatic interactions. What is more, Ag nanoparticles are deposited onto the binary photocatalyst by photo-assisted reduction. When the deposition amount of Ag nanoparticles is 3%, only a few Ag nanoparticles on the surface of MT are observed (Figure 5c). With the amount of Ag increasing, Figure 5d presents that more and more Ag nanoparticles decorate the MT. As the amount progressed to 8% in Figure 5e, we can see that MT is partially wrapped by RGO nanosheets, and Ag nanoparticles uniformly distribute on the other naked surface of MT. When continuing to add the amount of Ag, Ag nanoparticles have agglomerated easily into nanoclusters, and a similar phenomenon can also seen from Figure S1.

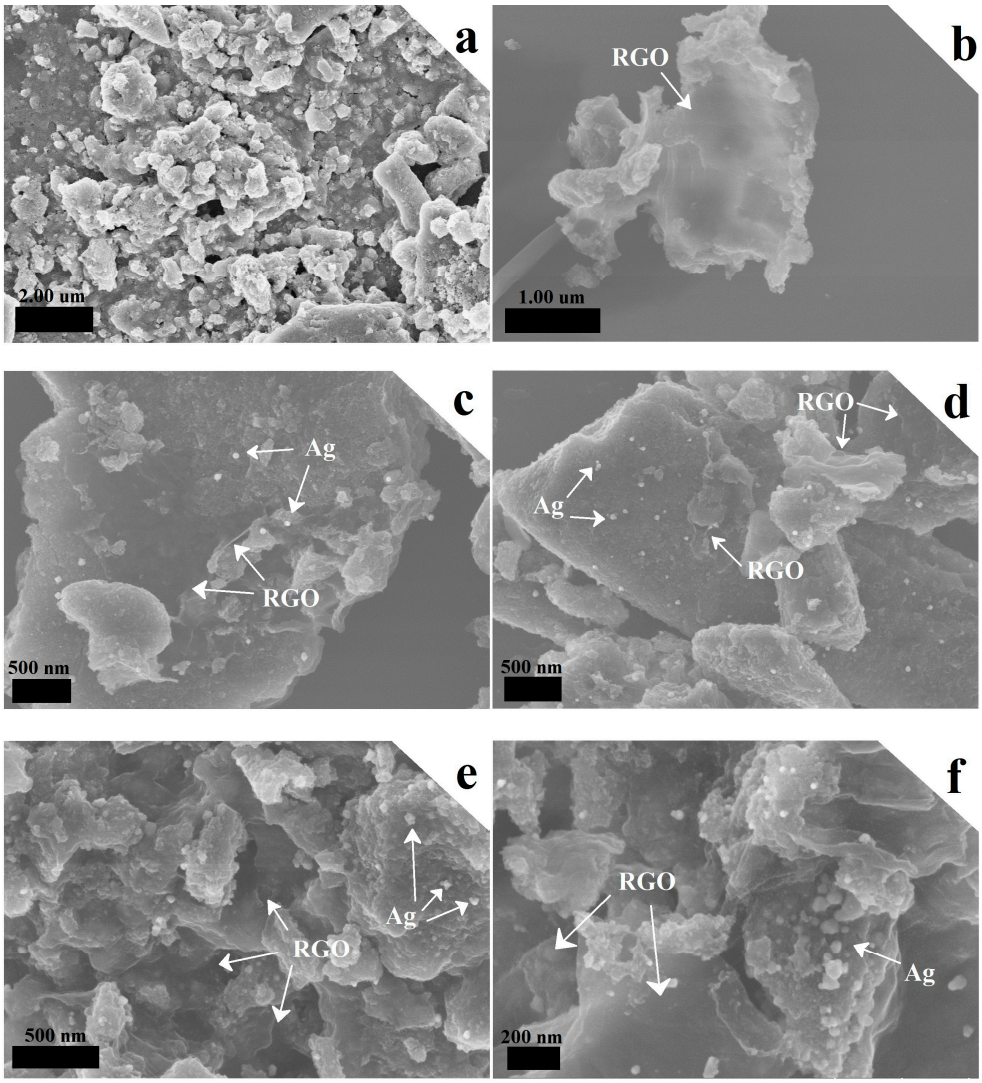

Figure 5. Field emission scanning electron microscope (FESEM) images of MT (**a**), MTG (**b**), MTGA-3 (**c**), MTGA-5 (**d**), MTGA-8 (**e**) and MTGA-10 (**f**) nanocomposites.

Figure 6 presents TEM and high-resolution transmission electron microscopy (HRTEM) images of MTGA nanocomposite, from which we can see that the TiO_2 nanocrystals modified by the Ag nanoparticles adhere to the chiffon-like RGO nanosheets, besides that TiO_2 possesses the mesoporous structure proven by Figure S2. The HRTEM image in Figure 6b unequivocally reveals that the specific interplanar spacings are 0.35 nm and 0.24 nm, respectively, belonging to the (101) facet of anatase TiO_2 and the (111) plane of a cubic phase Ag, which prove the coexistence of TiO_2 and Ag. Furthermore, Figure S4a–d displays the elemental mapping images based the selected area (Figure S3) on behalf of the Ti, O, C and Ag elements; it is further side evidence that Ag nanoparticles are deposited successfully by the photo-assisted process.

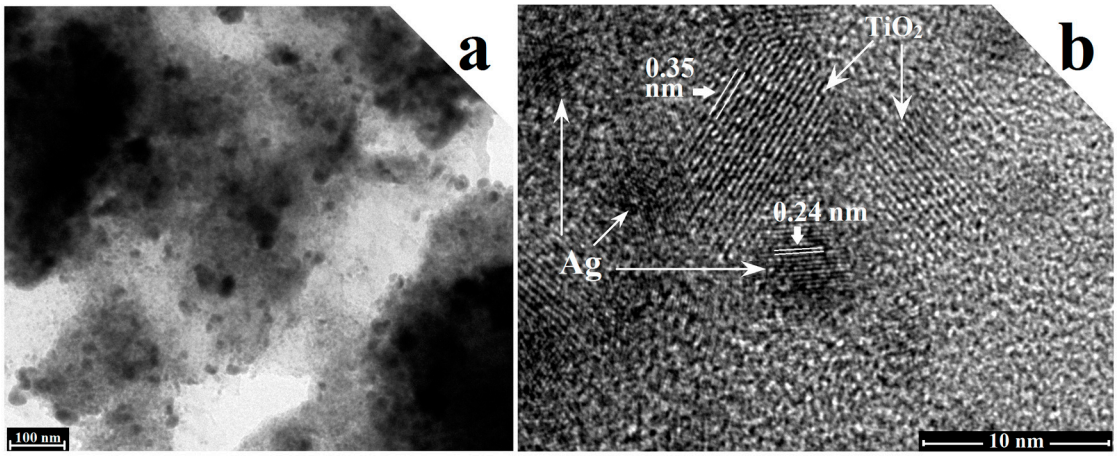

Figure 6. Transmission electron microscopy (TEM) (**a**) and high-resolution transmission electron microscopy (HRTEM) (**b**) images of the MTGA nanocomposite.

Ultraviolet-visible diffuse reflectance spectrum (UV/Vis DRS) measurements were performed to study the optical properties of the samples. As shown in Figure 7a, the pronounced absorption peak between 200 and 400 nm for all of the samples is ascribed to the electron excitation from the valence band to the conduction band of TiO_2 [45]. In comparison, the MTG nanocomposite exhibits a broadened, but weak absorbance within the visible-light region from 400 to 500 nm, which may come from the band-edge absorption of graphene. Notably, the absorption edge of MTGA exhibits an obvious red shift, and the absorption range is extended to the visible-light district because of the LSPR effect of Ag nanoparticles [22]. Moreover, a plot obtained via the conversion in view of the Kubelka–Munk function versus the energy of light is shown in Figure 7b, from which the band gap energy (Eg) of MT, MTG and MTGA nanocomposites is roughly estimated to be about 3.16 eV, 2.8 eV and 2.51 eV, respectively. This suggests that the decoration of Ag nanoparticles and RGO components with the TiO_2 have a significant impact on the absorption of visible light.

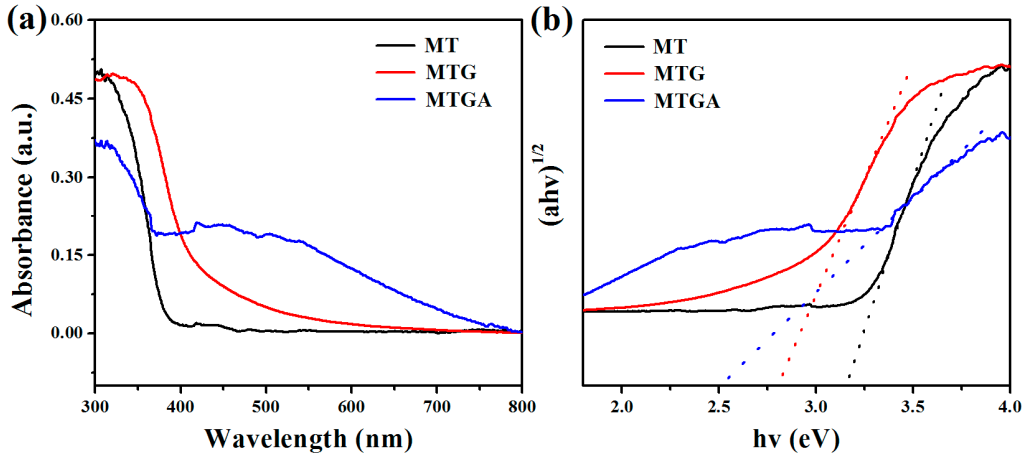

Figure 7. Ultraviolet-visible diffuse reflectance spectrum (UV/Vis DRS) (**a**) and a plot of transformed Kubelka–Munk function versus the energy of light (**b**) for MT, MTG and MTGA.

The photocatalytic performance of MT, MTG and MTGA was detected by the decomposition of MB dyes. As shown in Figure 8a, in the dark adsorption 30-min phase, with the increasing of silver content, the adsorption quantity is increasing until the amount reaches 8%. Following, under the condition of visible light, MB dye has self-degradation. Excluding the self-degradation, MT basically has no the

ability of degradation. Nevertheless, by contrast, MTG has a heightened photocatalytic activity to a certain extent, and MTGA presents the prominently highest photocatalytic activity, whereby when the illumination time is 120 min, the degradation rate of MTGA-8 reaches 93%, and the apparent reaction rate constant of the ternary material in Table S2 is 0.017 min^{-1}, which is almost 3.4-times the degradation rate of MTG; when silver content is added up to 10%, the degradation rate does not rise, rather being reduced because too much deposition of Ag nanoparticles themselves can become the recombination center that suppresses the carrier separation [51].

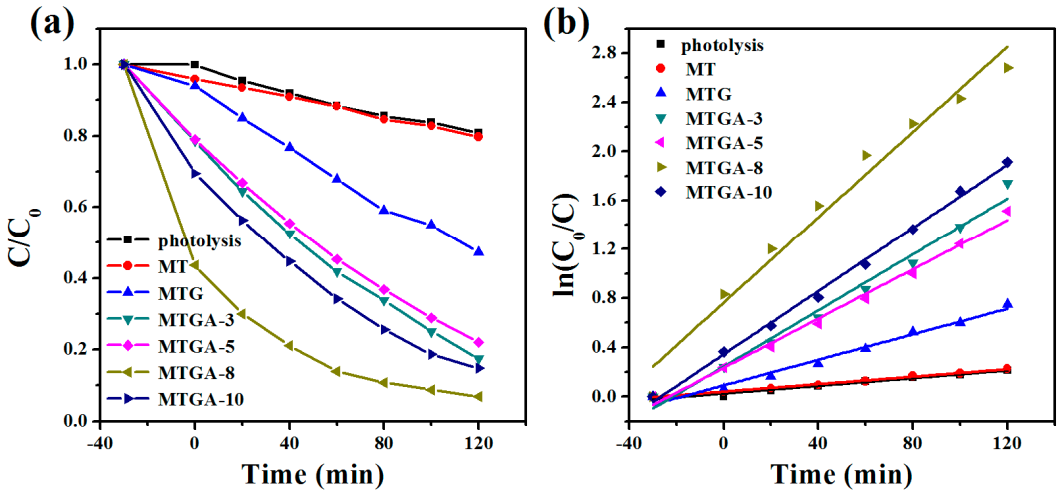

Figure 8. Photodegradation of methylene blue (MB) (**a**) and the apparent reaction rate constants k (**b**) in the presence of visible light of MT, MTG and MTGA (with different Ag loading values).

The stability of MTGA-8 is exhibited in Figure 9a; after three cycle times, the degradation rate reduces to 91.2%. Furthermore, the XRD spectrum of MTGA-8 after three cycle times shown in Figure 9b is also surveyed to determine whether the catalyst is deteriorated after the photocatalytic redox reaction. Compared to original MTGA-8, MTGA-8 after three cycle times remains as the typical anatase-phase TiO_2, and no peak of the other valence state of Ti appears. Furthermore, the peaks of Ag nanoparticles still are located at 38.1° and 44.2°, and the intensity of peaks is slightly weaker. What is more, XPS spectra for the MTGA nanocomposite in Figure S5 can also prove that the MTGA nanocomposite retains its composition after the photoreaction. Therefore, it is confirmed that MTGA exhibits an excellent photocatalytic capacity and high stability.

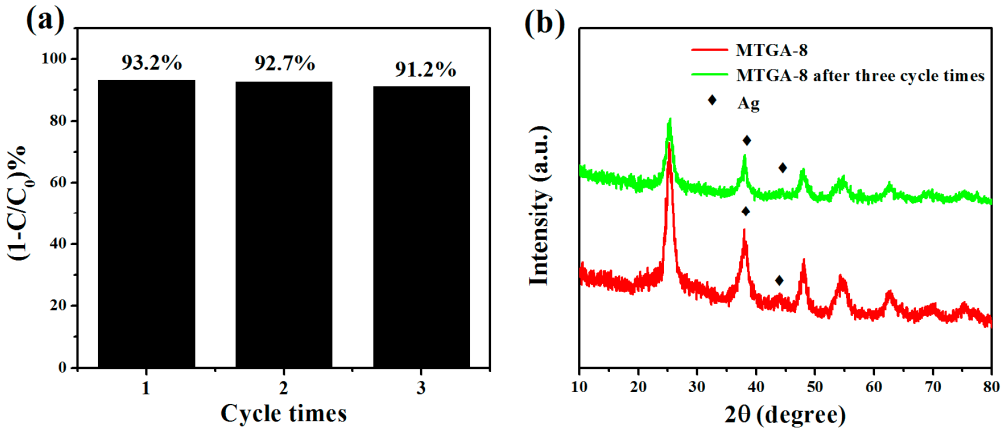

Figure 9. The cycle time of MTGA for degrading MB under visible light (**a**) and the XRD spectra of MTGA-8 and MTGA-8 after three cycle times (**b**).

In consideration of the above results, the boosted photocatalytic performance of MTGA ternary nanocomposite in the MB's decomposition can be attributed to the following factors: firstly, the decoration of Ag nanoparticles can form the LSPR effect to enhance the absorbance of the TiO_2 to visible light and offer a large number of electrons scattering to the CB of MT; secondly, TiO_2 with a mesoporous structure possesses a large specific surface area, increasing the adsorption of dyes; additionally, RGO nanosheets serve as the electron acceptors that effectively accelerate the separation efficiency of carriers and provide more active sites for the degradation reaction [52]; there is a potential and inseparable synergistic effect among MT, RGO and Ag that can facilitate the charge transfer and separation in MTGA nanocomposite.

To clarify the separation ability of the photogenerated carriers of MTGA, an electrochemical impedance spectroscopy (EIS) Nyquist plot has been performed to discuss electrons' separation and transfer [53,54]. As shown in Figure 10a, the typical electrochemical impedance spectra are presented as Nyquist plots, and it is observed that the semicircle of MTGA-8 is shorter than MTG's, which demonstrates the decrease of the solid state interface layer resistance and the charge transfer resistance on the surface [55]. Therefore, the construction of the ternary structure could suppress the charge recombination, and thereby, the MTGA nanocomposite exhibits the enhanced photocatalytic performance.

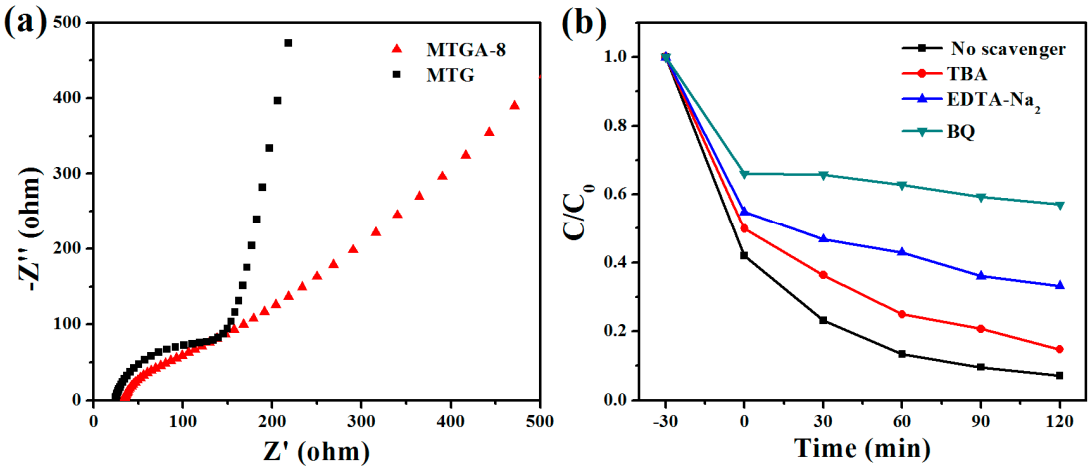

Figure 10. Electrochemical impedance spectroscopy (EIS) Nyquist impedance plots of MTG and MTGA-8 under visible light irradiation (**a**); photodegradation efficiency of MB with different scavengers under visible light irradiation (**b**).

On the other hand, to determine the dominating active species and expose the potential reaction mechanism of the MTGA ternary nanocomposite, a series of experiments adding different radical scavengers was carried out. In those experiments, tert butyl alcohol (TBA) as a hydroxyl radical (OH•) scavenger, ethylenediamine tetraacetic acid disodium salt (EDTA-Na_2) as a hole (h^+) scavenger and benzoquinone (BQ) as a superoxide radical ($O_2^{\bullet-}$) scavenger were joined into the photocatalytic system of the MTGA nanocomposite. Degradation efficiency of MB dye under these scavengers is shown in Figure 10b. In the dark adsorption 30-min phase, the adsorption efficiency of MB dye decreased as the reactive species scavenger was added, which may be on account of the competitive adsorption between MB and the additives [56]. When OH• scavenger (TBA) or h^+ scavenger (EDTA-Na_2) was added to the reaction system, the photocatalytic activity of MTGA obviously decreased from 93.4% down to 83.5% and 61.2%, respectively. When the $O_2^{\bullet-}$ scavenger (BQ) was added, eliminating the role of dark adsorption and self-degradation, MTGA towards degradation of the dye is basically ineffective. The above results illustrate that the OH•, h^+ and especially $O_2^{\bullet-}$ contribute to the high photocatalytic activity of MTGA for MB degradation. The most active radical is $O_2^{\bullet-}$, which may derive from the dissolved oxygen in the solution reacting with photoexcited electrons.

Based on the above analyses, a feasible photocatalytic mechanism over the MTGA ternary nanocomposite was proposed as depicted in Scheme 1. Under irradiation with visible light, Ag nanoparticles can work as an electron emitter to send out electrons (e^-) to the CB of MT. The electrons can transfer from the CB of TiO_2 to RGO nanosheets owing to the favorable energy level between the CB of the TiO_2 and the work function of RGO (0.08 V vs. normal hydrogen electrode (NHE) for the Fermi level) [57], in which RGO serves as an electron collector and transporter. During the transfer process, the electrons can react with the dissolved oxygen molecule (O_2) to get $O_2^{\bullet-}$, and H_2O and hydroxy (−OH) are absorbed by the rest of the h^+ of the holes of the Ag nanoparticles to obtain the •OH. Besides, h^+ itself has a strong oxidizing capacity. Therefore, $O_2^{\bullet-}$, h^+ and •OH can together promote the degradation of the dye. Without ignorance, the efficient electron transfer path among Ag nanoparticles, MT and RGO nanosheets can also play a synergistic interaction role, resulting in the significantly enhanced photoactivity of the MTGA ternary nanocomposite under visible light.

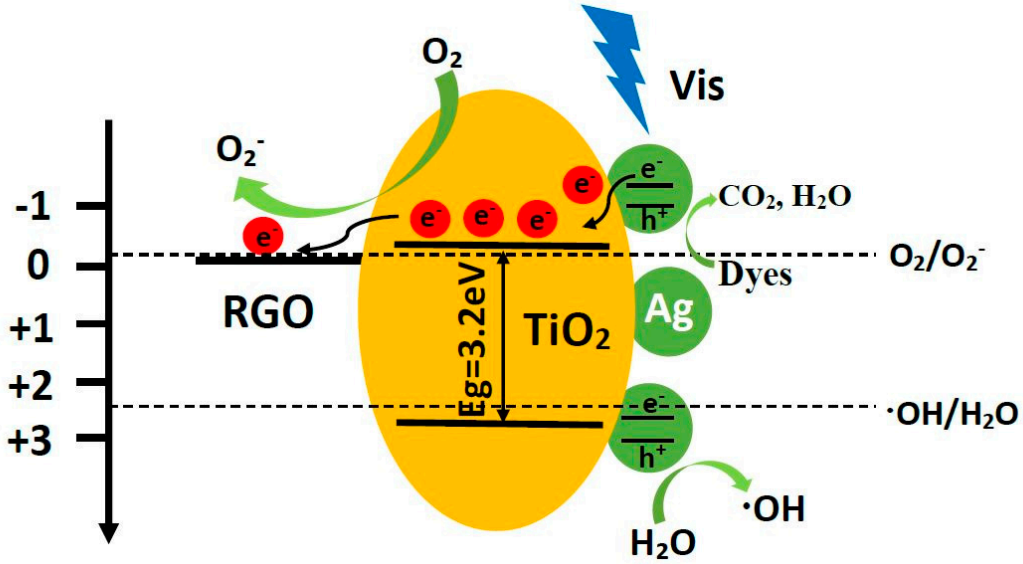

Scheme 1. Proposed mechanism diagram illustrating the photocatalytic redox reactions with the ternary MTGA catalyst in the presence of visible light.

3. Materials and Methods

3.1. Material

Pluronic@F-127 (EO96PO70EO96, MW = 12 000 g/mol) was purchased from Sigma-Aldrich, St. Louis, MO, USA. Tetrabutyl titanate (TBOT), acetic acid ($C_2H_4O_2$), hydrogen peroxide (H_2O_2, 30%), silver nitrate ($AgNO_3$) and 3-aminopropyl-trimethoxysilane (APTES) were supplied by Sinopharm (Shanghai, China). Nitric acid (HNO_3), sulfuric acid (H_2SO_4), hydrochloric acid (HCl) and ethanol (C_2H_6O) were obtained from Beijing Chemical Works, Beijing, China. Graphite powder was provided from Alfa Aesar China, Tianjin, China. All of the materials were used without further purification. The deionized (DI) water used in these experiments was obtained from local sources.

3.2. Synthesis

3.2.1. Synthesis of GO

GO was produced from natural graphite fakes by a modified Hummers method [58–60]. In a typical experiment, 1 g graphite powder and 1 g $NaNO_3$ were added to 33 mL concentrated H_2SO_4 in a 3 °C ice-bath. Then, 6 g ground $KMnO_4$ was slowly added while stirring. Then, the mixture was stirred for 1.5 h at 35 °C, with slowly adding 40 mL distilled water to the mixture. The obtained

mixture was stirred for a further 35 min at 90 °C. In the end, 100 mL distilled water were added to the mixture and 30 wt % H_2O_2 dropped gradually into it until the mixture turned bright yellow. Then, the mixture was washed with 150 mL 5% aqueous HCl to get rid of the metal ions, followed by washing with distilled water to effectively remove any remaining metal ions and acids. Finally, the resultant mixture was put into a vacuum drying oven at 60 °C. After 24 h, the brown exfoliated graphite oxide was obtained.

3.2.2. Synthesis of MT

MT was obtained via the template method based on Fan's work with modifications [61]. In a typical sol-gel process, 1.6 g of F-127 was dissolved in 30 mL of ethanol by stirring for 30 min, and then 2.3 mL HOAc, 1.8 mL HNO_3 and 3.4 mL TBOT were added stepwise. The mixed solution was stirred continuously for 1 h and then poured into a 120-mm Petri dish. Then, the Petri dish was placed in an oven at 40 °C for 12 h to form a transparent membrane, followed by ageing at 65 °C for 24 h. Finally, the as-prepared membranes were calcined at 350 °C in an air atmosphere for 5 h (heating rate 2 °C min^{-1}) to eventually obtain MT.

3.2.3. Synthesis of MTG and MTGA Nanocomposites

The MTGA nanocomposites were prepared by a photo-assisted reduction method [29,58]. Typically, 0.1 g MT were dispersed into 20 mL ethanol. Then, 1 mL of 3-aminopropyl-trimethoxysilane (APTES) was added, and the suspension was refluxed at 80 °C for 4 h. Subsequently, the suspension was washing three times with ethanol. Afterwards, the APTES-modified MT was added into 5.26 mg GO suspension after ultrasonication with stirring for 30 min to obtain a meso-TiO_2/GO suspension. The as-obtained meso-TiO_2/GO suspension and $AgNO_3$ were dispersed in ethanol and transferred to a glass reactor. Subsequently, the glass reactor containing the suspension kept at room temperature was exposed to the simulated solar light for 2 h. Then, the suspension was rinsed with ethanol and water a few times. Finally, the resultant was dried at 60 °C overnight. Similarly, MTG was synthesized by a photo-reduction in which the meso-TiO_2/GO suspension was dispersed in ethanol, and the above steps were repeated. Finally, we obtained the MTG and MTGA-x (x = 3, 5, 8 and 10), where x indicates the mass ratio of Ag loaded onto MT.

3.3. Characterization

The as-obtained catalysts were examined by an X-ray diffractometer (XRD) with Cu Kα radiation. The Raman spectra were surveyed by laser confocal micro-Raman spectroscopy with an excitation wavelength of 532 nm. X-ray photoelectron spectroscopy (XPS) measurements were conducted on a Thermo ESCALAB 250 spectrometer with a hemisphere detector at an energy resolution of 0.1 eV offered by an Al Kα radiation source. Field emission scanning electron microscope (FESEM) images were obtained by a Hitachi SU8010 machine. Transmission electron microscopy (TEM) and high-resolution transmission electron microscopy (HRTEM) images were obtained by a JEOL Model JEM-2100F instrument operated at 200 kV. The Brunauer–Emmett–Teller (BET) specific surface areas of the sample powders were obtained through nitrogen adsorption-desorption, measured on a JW-BK132F. Ultraviolet-visible (UV/Vis) absorption spectra were surveyed using a UV/Vis spectrometer (UV-2500, Shimadzu, Kyoto, Japan), in which $BaSO_4$ was chosen as the reference standard. The electrochemical analysis was investigated by a conventional three-electrode system measured on a CHI660E.

3.4. Photocatalytic Activity

The photocatalytic degradation reaction is based on a semiconductor photocatalyst that oxidizes the target contaminants to convert to H_2O and CO_2 under visible light irradiation. In this experiment, an amount of photocatalyst was added to 10 mg/L MB solution under normal temperature and pressure. After a few minutes, the dark reaction was carried out for 30 min to allow the photocatalyst to reach the desorption equilibrium and then transferred to the photocatalytic reaction device.

Opening the light source (xenon lamp 300 W), taking 4 mL degradation solution every 20 min, centrifuging at 5000 r/min speed for 5–10 min, the supernatant was placed in a quartz cuvette; the use of the UV/Vis spectrophotometer scanned in the wavelength range of 300–800 nm was performed to determine the absorbance of the indicator solution after degradation. MB solution is at 664 nm to reach the maximum absorbance. The absorbance of the indicator solution will change after degradation, and the change of the concentration can be calculated by the absorbance rate. The photocatalytic efficiency of the photocatalyst to the indicator solution is deduced.

In addition, a series of control experiments using different radical scavengers (i.e., TBA as a hydroxyl radical (OH•) scavenger, EDTA-Na_2 as a hole (h^+) scavenger and BQ as a superoxide radical ($O_2^{\bullet-}$) scavenger) for the photodegradation of an aqueous solution of MB under visible light irradiation was performed in an analogous way.

4. Conclusions

The ternary nanocomposite of mesoporous TiO_2/RGO/Ag has been successfully synthesized by an electrostatic self-assembly approach and a photo-assisted reduction process. Moreover, the ternary MTGA exhibited superior photocatalytic activity; for the degradation of MB under visible light, the degradation rate reached up to 0.017 min^{-1}, which was 3.4-times that of MTG. What is more, the degradation rate of the MTGA nanocomposite after three cycle times is 91.2%, and the composition is unchanged. In addition, we found that the OH•, h^+ and especially $O_2^{\bullet-}$ contribute to the high photocatalytic activity of MTGA for MB degradation. It is worth noting that the possible electron transfer route is that the Ag nanoparticles work as an electron emitter to send out the electrons to the CB of MT, following RGO nanosheets that can receive electrons to effectively separate electrons and holes. Additionally, the enhanced photocatalytic activity depends on the synergistic effect among the individual constituents of the catalyst. Therefore, the MTGA ternary nanocomposite is potentially useful as a catalyst towards photodegradation of organic pollutants.

Supplementary Materials: The following are available online at www.mdpi.com/2073-4344/7/5/156/s1, Table S1: Textural properties of MT, MTG and MTGA-8 nanocomposites; Table S2: The apparent reaction rate constants k in the presence of visible light of MT, MTG and MTGA nanocomposites; Figure S1: TEM images of MT (a), MTG (b), MTGA-3 (c), MTGA-5 (d), MTGA-8 (e) and MTGA-10 (f); Figure S2: XRD pattern in small-angle (a), nitrogen sorption isotherm (b) and the corresponding pore size distribution curve (inset) for MT; Figure S3: The selected pattern with the elemental mapping of the MTGA-8 nanocomposite; Figure S4: The corresponding elemental mapping images of Ti (a), O (b), C (c) and Ag (d); Figure S5: XPS survey spectrum of the MTGA-8 nanocomposite; Figure S6: The mass of MB before and after degradation.

Acknowledgments: Financial support from the National Natural Science Foundation of China (No. 51472106) and the Key Project of Science and Technology of The Jilin Provincial Education Department during the 13th Five-Year Plan Period are highly appreciated.

Author Contributions: C.X.W., H.W.T. and X.Y.W. conceived of and designed the experiments and collected the data. X.X. and X.H. analyzed the data and discussed the results. C.X.W. and H.W.T. wrote the paper. All authors discussed the results and commented on the manuscript.

Conflicts of Interest: The authors declare no conflict of interest.

References

1. Kumar, S.G.; Devi, L.G. Review on modified TiO_2 photocatalysis under uv/visible light: Selected results and related mechanisms on interfacial charge carrier transfer dynamics. *J. Phys. Chem. A* **2011**, *115*, 13211–13241. [CrossRef] [PubMed]
2. Hu, X.L.; Li, G.S.; Yu, J.C. Design, fabrication, and modification of nanostructured semiconductor materials for environmental and energy applications. *Langmuir* **2010**, *26*, 3031–3039. [CrossRef] [PubMed]
3. Yan, K.; Wu, G.; Jarvis, C.; Wen, J.; Chen, A. Facile synthesis of porous microspheres composed of TiO_2 nanorods with high photocatalytic activity for hydrogen production. *Appl. Catal. B Environ.* **2014**, *148–149*, 281–287. [CrossRef]
4. Liu, S.W.; Yu, J.G.; Cheng, B.; Jaroniec, M. Fluorinated semiconductor photocatalysts: Tunable synthesis and unique properties. *Adv. Colloid Interface Sci.* **2012**, *173*, 35–53. [CrossRef] [PubMed]

5. Liu, G.; Wang, L.Z.; Yang, H.G.; Cheng, H.M.; Lu, G.Q. Titania-based photocatalysts-crystal growth, doping and heterostructuring. *J. Mater. Chem.* **2010**, *20*, 831–843. [CrossRef]
6. Yang, H.G.; Sun, C.H.; Qiao, S.Z.; Zou, J.; Liu, G.; Smith, S.C.; Cheng, H.M.; Lu, G.Q. Anatase TiO_2 single crystals with a large percentage of reactive facets. *Nature* **2008**, *453*, 638–641. [CrossRef] [PubMed]
7. Dozzi, M.V.; Selli, E. Specific facets-dominated anatase TiO_2: Fluorine-mediated synthesis and photoactivity. *Catalysts* **2013**, *3*, 455–485. [CrossRef]
8. Yan, K.; Wu, G. Titanium dioxide microsphere-derived materials for solar fuel hydrogen generation. *ACS Sustain. Chem. Eng.* **2015**, *3*, 779–791. [CrossRef]
9. Yu, Y.; Yu, J.C.; Yu, J.G.; Kwok, Y.C.; Che, Y.K.; Zhao, J.C.; Ding, L.; Ge, W.K.; Wong, P.K. Enhancement of photocatalytic activity of mesoporous TiO2 by using carbon nanotubes. *Appl. Catal. A Gen.* **2005**, *289*, 186–196. [CrossRef]
10. Yu, J.G.; Ma, T.T.; Liu, S.W. Enhanced photocatalytic activity of mesoporous TiO_2 aggregates by embedding carbon nanotubes as electron-transfer channel. *Phys. Chem. Chem. Phys.* **2011**, *13*, 3491–3501. [CrossRef] [PubMed]
11. Williams, G.; Seger, B.; Kamat, P.V. TiO_2-graphene nanocomposites. Uv-assisted photocatalytic reduction of graphene oxide. *Acs Nano* **2008**, *2*, 1487–1491. [CrossRef] [PubMed]
12. Li, G.S.; Zhang, D.Q.; Yu, J.C. A new visible-light photocatalyst: Cds quantum dots embedded mesoporous TiO_2. *Environ. Sci. Technol.* **2009**, *43*, 7079–7085. [CrossRef] [PubMed]
13. Ge, M.Z.; Cao, C.Y.; Li, S.H.; Tang, Y.X.; Wang, L.N.; Qi, N.; Huang, J.Y.; Zhang, K.Q.; Al-Deyab, S.S.; Lai, Y.K. In situ plasmonic ag nanoparticle anchored TiO_2 nanotube arrays as visible-light-driven photocatalysts for enhanced water splitting. *Nanoscale* **2016**, *8*, 5226–5234. [CrossRef] [PubMed]
14. Tian, H.; Shen, K.; Hu, X.; Qiao, L.; Zheng, W. N s co-doped graphene quantum dots-graphene-TiO_2 nanotubes composite with enhanced photocatalytic activity. *J. Alloys Compd.* **2017**, *691*, 369–377. [CrossRef]
15. Xie, C.; Yang, S.H.; Shi, J.W.; Niu, C.M. Highly crystallized c-doped mesoporous anatase TiO_2 with visible light photocatalytic activity. *Catalysts* **2016**, *6*, 117. [CrossRef]
16. Eda, G.; Fanchini, G.; Chhowalla, M. Large-area ultrathin films of reduced graphene oxide as a transparent and flexible electronic material. *Nat. Nanotechnol.* **2008**, *3*, 270–274. [CrossRef] [PubMed]
17. Stankovich, S.; Dikin, D.A.; Dommett, G.H.B.; Kohlhaas, K.M.; Zimney, E.J.; Stach, E.A.; Piner, R.D.; Nguyen, S.T.; Ruoff, R.S. Graphene-based composite materials. *Nature* **2006**, *442*, 282–286. [CrossRef] [PubMed]
18. Xiang, Q.; Yu, J.; Jaroniec, M. Graphene-based semiconductor photocatalysts. *Chem. Soc. Rev.* **2012**, *41*, 782–796. [CrossRef] [PubMed]
19. Wang, W.G.; Yu, J.G.; Xiang, Q.J.; Cheng, B. Enhanced photocatalytic activity of hierarchical macro/mesoporous TiO_2-graphene composites for photodegradation of acetone in air. *Appl. Catal. B Environ.* **2012**, *119*, 109–116. [CrossRef]
20. Zhang, H.; Lv, X.J.; Li, Y.M.; Wang, Y.; Li, J.H. P25-graphene composite as a high performance photocatalyst. *Acs Nano* **2010**, *4*, 380–386. [CrossRef] [PubMed]
21. Liu, J.C.; Bai, H.W.; Wang, Y.J.; Liu, Z.Y.; Zhang, X.W.; Sun, D.D. Self-assembling TiO_2 nanorods on large graphene oxide sheets at a two-phase interface and their anti-recombination in photocatalytic applications. *Adv. Funct. Mater.* **2010**, *20*, 4175–4181. [CrossRef]
22. He, X.L.; Cai, Y.Y.; Zhang, H.M.; Liang, C.H. Photocatalytic degradation of organic pollutants with ag decorated free-standing TiO_2 nanotube arrays and interface electrochemical response. *J. Mater. Chem.* **2011**, *21*, 475–480. [CrossRef]
23. Ismail, A.A. Facile synthesis of mesoporous ag-loaded TiO_2 thin film and its photocatalytic properties. *Microporous Mesoporous Mater.* **2012**, *149*, 69–75. [CrossRef]
24. Sellappan, R.; Nielsen, M.G.; Gonzalez Posada, F.; Vesborg, P.C.K.; Chorkendorff, I.; Chakarov, D. Effects of plasmon excitation on photocatalytic activity of ag/TiO_2 and au/TiO_2 nanocomposites. *J. Catal.* **2013**, *307*, 214–221. [CrossRef]
25. Sher Shah, M.S.; Zhang, K.; Park, A.R.; Kim, K.S.; Park, N.G.; Park, J.H.; Yoo, P.J. Single-step solvothermal synthesis of mesoporous ag-TiO_2-reduced graphene oxide ternary composites with enhanced photocatalytic activity. *Nanoscale* **2013**, *5*, 5093–5101. [CrossRef] [PubMed]
26. Kumar, R.; El-Shishtawy, R.M.; Barakat, M.A. Synthesis and characterization of ag-ag_2o/TiO_2@polypyrrole heterojunction for enhanced photocatalytic degradation of methylene blue. *Catalysts* **2016**, *6*, 67. [CrossRef]

27. Xian, J.J.; Li, D.Z.; Chen, J.; Li, X.F.; He, M.; Shao, Y.; Yu, L.H.; Fang, J.L. Tio_2 nanotube array-graphene-cds quantum dots composite film in z-scheme with enhanced photoactivity and photostability. *ACS Appl. Mater. Interfaces* **2014**, *6*, 13157–13166. [CrossRef] [PubMed]
28. Myilsamy, M.; Murugesan, V.; Mahalakshmi, M. Indium and cerium co-doped mesoporous TiO_2 nanocomposites with enhanced visible light photocatalytic activity. *Appl. Catal. A Gen.* **2015**, *492*, 212–222. [CrossRef]
29. Li, W.Q.; Liu, X.; Li, H.X. Hydrothermal synthesis of graphene/Fe^{3+}-doped TiO_2 nanowire composites with highly enhanced photocatalytic activity under visible light irradiation. *J. Mater. Chem. A* **2015**, *3*, 15214–15224. [CrossRef]
30. Lin, X.; Xu, D.; Lin, Z.; Jiang, S.S.; Chang, L.M. Construction of heterostructured TiO_2/$invo_4$/rgo microspheres with dual-channels for photo-generated charge separation. *RCS Adv.* **2015**, *5*, 84372–84380. [CrossRef]
31. Li, L.; Wu, B.H.; Li, G.N.; Li, Y.S. C, n co-doping promoted mesoporous au/TiO_2 catalyst for low temperature co oxidation. *RSC Adv.* **2016**, *6*, 28904–28911. [CrossRef]
32. Xue, C.; Yan, X.; Ding, S.; Yang, G. Monodisperse ag–agbr nanocrystals anchored on one-dimensional TiO_2 nanotubes with efficient plasmon-assisted photocatalytic performance. *RSC Adv.* **2016**, *6*, 68653–68662. [CrossRef]
33. Wen, Y.; Ding, H.; Shan, Y. Preparation and visible light photocatalytic activity of ag/TiO_2/graphene nanocomposite. *Nanoscale* **2011**, *3*, 4411–4417. [CrossRef] [PubMed]
34. Khalid, N.R.; Ahmed, E.; Ahmad, M.; Niaz, N.A.; Ramzan, M.; Shakil, M.; Iqbal, T.; Majid, A. Microwave-assisted synthesis of ag-TiO_2/graphene composite for hydrogen production under visible light irradiation. *Ceram. Int.* **2016**, *42*, 18257–18263. [CrossRef]
35. Wang, Y.; Tang, Y.H.; Chen, Y.; Li, Y.; Liu, X.N.; Luo, S.L.; Liu, C.B. Reduced graphene oxide-based photocatalysts containing ag nanoparticles on a TiO_2 nanotube array. *J. Mater. Sci.* **2013**, *48*, 6203–6211. [CrossRef]
36. Rosu, M.C.; Socaci, C.; Floare-Avram, V.; Borodi, G.; Pogacean, F.; Coros, M.; Magerusan, L.; Pruneanu, S. Photocatalytic performance of graphene/TiO_2-ag composites on amaranth dye degradation. *Mater. Chem. Phys.* **2016**, *179*, 232–241. [CrossRef]
37. Zhang, J.; Xiao, F.X.; Xiao, G.; Liu, B. Self-assembly of a ag nanoparticle-modified and graphene-wrapped TiO_2 nanobelt ternary heterostructure: Surface charge tuning toward efficient photocatalysis. *Nanoscale* **2014**, *6*, 11293–11302. [CrossRef] [PubMed]
38. Gou, X.L.; Cheng, Y.L.; Liu, B.; Yang, B.J.; Yan, X.B. Fabrication and photocatalytic properties of TiO_2/reduced graphene oxide/ag nanocomposites with uv/vis response. *Eur. J. Inorg. Chem.* **2015**, 2222–2228. [CrossRef]
39. Vasilaki, E.; Georgaki, I.; Vernardou, D.; Vamvakaki, M.; Katsarakis, N. Ag-loaded TiO_2/reduced graphene oxide nanocomposites for enhanced visible-light photocatalytic activity. *Appl. Surf. Sci.* **2015**, *353*, 865–872. [CrossRef]
40. Zhang, L.; Ni, C.; Jiu, H.; Xie, C.; Yan, J.; Qi, G. One-pot synthesis of ag-TiO_2/reduced graphene oxide nanocomposite for high performance of adsorption and photocatalysis. *Ceram. Int.* **2017**, *43*, 5450–5456. [CrossRef]
41. Leong, K.H.; Sim, L.C.; Bahnemann, D.; Jang, M.; Ibrahim, S.; Saravanan, P. Reduced graphene oxide and ag wrapped TIO_2 photocatalyst for enhanced visible light photocatalysis. *APL Mater.* **2015**, *3*, 104503. [CrossRef]
42. Tian, H.; Wan, C.; Zheng, W.; Hu, X.; Qiao, L.; Wang, X. Construction of a ternary hybrid of cds nanoparticles loaded on mesoporous-TiO_2/rgo for the enhancement of photocatalytic activity. *RSC Adv.* **2016**, *6*, 84722–84729. [CrossRef]
43. Liu, S.W.; Liu, C.; Wang, W.G.; Cheng, B.; Yu, J.G. Unique photocatalytic oxidation reactivity and selectivity of TiO_2-graphene nanocomposites. *Nanoscale* **2012**, *4*, 3193–3200. [CrossRef] [PubMed]
44. Xiao, F. An efficient layer-by-layer self-assembly of metal-TiO_2 nanoring/nanotube heterostructures, m/t-nrnt (m = au, ag, pt), for versatile catalytic applications. *Chem. Commun.* **2012**, *48*, 6538–6540. [CrossRef] [PubMed]
45. Xiao, F. Layer-by-layer self-assembly construction of highly ordered metal-TiO_2 nanotube arrays heterostructures (m/tnts, m = au, ag, pt) with tunable catalytic activities. *J. Phys. Chem. C* **2012**, *116*, 16487–16498. [CrossRef]

46. Xiao, F.X.; Miao, J.; Liu, B. Self-assembly of aligned rutile@anatase TiO_2 nanorod@cds quantum dots ternary core-shell heterostructure: Cascade electron transfer by interfacial design. *Mater. Horiz.* **2014**, *1*, 259–263. [CrossRef]
47. Benedetti, J.E.; Bernardo, D.R.; Morais, A.; Bettini, J.; Nogueira, A.F. Synthesis and characterization of a quaternary nanocomposite based on TiO_2/cds/rgo/pt and its application in the photoreduction of CO_2 to methane under visible light. *RSC Adv.* **2015**, *5*, 33914–33922. [CrossRef]
48. Pan, X.Y.; Xu, Y.J. Graphene-templated bottom-up fabrication of ultralarge binary cds-TiO_2 nanosheets for photocatalytic selective reduction. *J. Phys. Chem. C* **2015**, *119*, 7184–7194. [CrossRef]
49. Zhang, Y.H.; Tang, Z.R.; Fu, X.; Xu, Y.J. Engineering the unique 2d mat of graphene to achieve graphene-TiO_2 nanocomposite for photocatalytic selective transformation: What advantage does graphene have over its forebear carbon nanotube? *ACS Nano* **2011**, *5*, 7426–7435. [CrossRef] [PubMed]
50. Zhang, Y.H.; Zhang, N.; Tang, Z.R.; Xu, Y.J. Graphene transforms wide band gap zns to a visible light photocatalyst. The new role of graphene as a macromolecular photosensitizer. *ACS Nano* **2012**, *6*, 9777–9789. [CrossRef] [PubMed]
51. Grabowska, E.; Zaleska, A.; Sorgues, S.; Kunst, M.; Etcheberry, A.; Colbeaujustin, C.; Remita, H. Modification of titanium(iv) dioxide with small silver nanoparticles: Application in photocatalysis. *J. Phys. Chem. C* **2013**, *117*, 1955–1962. [CrossRef]
52. Fan, W.Q.; Yu, X.Q.; Lu, H.C.; Bai, H.Y.; Zhang, C.; Shi, W.D. Fabrication of TiO_2/rgo/Cu_2O heterostructure for photoelectrochemical hydrogen production. *Appl. Catal. B Environ.* **2016**, *181*, 7–15. [CrossRef]
53. Xiao, F.X.; Miao, J.W.; Liu, B. Layer-by-layer self-assembly of cds quantum dots/graphene nanosheets hybrid films for photoelectrochemical and photocatalytic applications. *J. Am. Chem. Soc.* **2014**, *136*, 1559–1569. [CrossRef] [PubMed]
54. Tang, Z.R.; Yin, X.; Zhang, Y.H.; Xu, Y.J. Synthesis of titanate nanotube-cds nanocomposites with enhanced visible light photocatalytic activity. *Inorg. Chem.* **2013**, *52*, 11758–11766. [CrossRef] [PubMed]
55. He, B.L.; Dong, B.; Li, H.L. Preparation and electrochemical properties of ag-modified TiO_2 nanotube anode material for lithium-ion battery. *Electrochem. Commun.* **2007**, *9*, 425–430. [CrossRef]
56. Chen, X.J.; Dai, Y.Z.; Wang, X.Y.; Guo, J.; Liu, T.H.; Li, F.F. Synthesis and characterization of ag(3)po(4) immobilized with graphene oxide (go) for enhanced photocatalytic activity and stability over 2,4-dichlorophenol under visible light irradiation. *J. Hazard. Mater.* **2015**, *292*, 9–18. [CrossRef] [PubMed]
57. Wang, X.W.; Tian, H.W.; Cui, X.Q.; Zheng, W.T.; Liu, Y.C. One-pot hydrothermal synthesis of mesoporous $zn_xcd_{1-x}s$/reduced graphene oxide hybrid material and its enhanced photocatalytic activity. *Dalton Trans.* **2014**, *43*, 12894–12903. [CrossRef] [PubMed]
58. Stankovich, S.; Dikin, D.A.; Piner, R.D.; Kohlhaas, K.A.; Kleinhammes, A.; Jia, Y.; Wu, Y.; Nguyen, S.T.; Ruoff, R.S. Synthesis of graphene-based nanosheets via chemical reduction of exfoliated graphite oxide. *Carbon* **2007**, *45*, 1558–1565. [CrossRef]
59. Park, S.; Ruoff, R.S. Chemical methods for the production of graphenes. *Nat. Nanotechnol.* **2009**, *4*, 217–224. [CrossRef] [PubMed]
60. Zhu, Y.; Murali, S.; Cai, W.; Li, X.; Suk, J.W.; Potts, J.R.; Ruoff, R.S. Graphene and graphene oxide: Synthesis, properties, and applications. *Adv. Mater.* **2010**, *22*, 3906–3924. [CrossRef] [PubMed]
61. Fan, J.; Boettcher, S.W.; Stucky, G.D. Nanoparticle assembly of ordered multicomponent mesostructured metal oxides via a versatile sol-gel process. *Chem. Mater.* **2006**, *18*, 6391–6396. [CrossRef]